Computational Materials Science 95 (2014) 408–413

Contents lists available at ScienceDirect

Computational Materials Science

journal homepage: www.elsevier.com/locate/commatsci

Experimental observation and numerical simulation of SiC_{3D}/Al interpenetrating phase composite material subjected to a three-point bending load

Linlin Wang, Qunbo Fan *, Guoju Li, Hongmei Zhang, Fuchi Wang

National Key Laboratory of Science and Technology on Materials under Shock and Impact, School of Materials Science and Engineering, Beijing Institute of Technology, Beijing 100081, China

ARTICLE INFO

Article history:
Received 7 May 2014
Received in revised form 16 July 2014
Accepted 5 August 2014

Keywords:
Interpenetrating phase composite
SiC_{3D}/Al
Three-point bending
Failure mechanism

ABSTRACT

The failure process and the underlying mechanism of crack initiation, crack propagation and eventual fracture of SiC_{3D}/Al interpenetrating phase composite subjected to a static three-point bending load were investigated using in-situ SEM observation and two-dimensional microstructure-embedded numerical simulation. It was found that stress concentration originally occurred in the SiC ceramic phase near the bottom of the specimen, causing horizontal tensile forces and inducing a vertical microcrack inside the SiC phase near the SiC–Al interface. With increased load, more microcracks were gradually initiated in the SiC phase, and severe tearing plastic deformation and cracking of the Al phase occurred at the base of the specimen. Subsequently, the microcracks propagated and connected to form a primary crack. It was notable that at the final stage of the primary crack, cracking in the Al phase no longer occurred due to the sudden release of the internal energy in the composite material. Interestingly, the primary crack bridged over the Al phase then continued to propagate in the SiC material. Simulated results were consistent with observed behavior.

1. Introduction

Interpenetrating phase composites (IPCs) are a type of composite material in which both the matrix and reinforcement phase are continuous, interpenetrating three dimensionally throughout the microstructure. Consequently, many of the more attractive properties of each constituent phase may be retained in the composite product [1]. In the present case, the stiffness of ceramic/metal IPCs was found to be superior to that of metals, and their toughness and structural integrity were superior to those of monolithic ceramic materials [2]. The potentially broad range of applications in various fields have made IPCs the focus of significant research activity in recent years.

Some works have investigated the production, characterization and modeling of IPCs [3–7]. Breslin et al. [8] used the liquid phase displacement reaction method to produce an aluminum/alumina IPC with enhanced density, thermal conductivity and coefficient of thermal expansion characteristics, without compromising stiffness or fracture toughness. Vaucher et al. [9] prepared a series of SiOC ceramic foams, in which the cell size was shown to influence the mechanical properties of the composite, and were improved by reducing the size of the pore formers. Wegner and Gibson [10] reported on a modeling investigation of the mechanical and thermal expansion properties of one specific IPC: a stainless steel/bronze composite. Numerical results showed that the presence of thermal residual stresses and porosity contributed to a reduction in its effective elastic modulus.

Because of the potential advantages of IPCs, substantial research effort has been directed towards a better understanding of their behavior, especially their fracture behavior, under different loading conditions [11]. The unique reinforcement structure of IPCs produces a fracture behavior that is much more complex than that of traditional composites [2,12]. Prielipp et al. [13] measured fracture strength and fracture toughness of an aluminum/alumina interpenetrating composite as a function of ligament diameter and volume fraction of the metal reinforcement. Metal-reinforced interpenetrating composites have consistently been found to have higher fracture strengths. Some studies have observed the behavior of the material using an in situ scanning electron microscope (SEM); for example, Zhou et al. [14] investigated the fracture behavior of Al_2O_3–TiC/Al metal–matrix interpenetrating phase composite (MMIPC) by in-situ SEM observation and found that a very good interfacial bond strength was developed between the

* Corresponding author. Tel.: +86 10 68911144 863; fax: +86 10 68911144 866.
E-mail address: fanqunbo@bit.edu.cn (Q. Fan).

http://dx.doi.org/10.1016/j.commatsci.2014.08.008
0927-0256/

matrix and the reinforcements. In brittle ceramic materials, however, cracks propagate rapidly and the material immediately fractures. In such a case, crack initiation and propagation is not readily recorded. A literature survey on this topic indicates that little work has yet been done to reveal the underlying mechanism of the fracture process of IPCs, and numerical simulations are still at a preliminary stage.

In recent years, some researchers, such as Dai and You [15] and Shen [16], had paid their attentions to a novel method of building finite element model called digital image processing technique, which can accurately capture the real microstructures of complex composites for a reliable simulation of their failure process. Similarly, in our research, to better understand the nature of the crack growth, digital image processing technique combined with the finite element (FE) method was also employed to build a two-dimensional (2D) micromodel based on the actual characteristics of SiC_{3D}/Al microstructures. In addition, in order to reduce the computing cost, the best solution is to construct a microstructure-embedded model combining macroscale and microscale, in which the macromodel is used in the region far away from the crack and the micromodel is employed near its vicinity [17]. Such methods can greatly reduce the computing burden, but does not reduce the reliability of computational results. By this means, the fracture process of SiC_{3D}/Al interpenetrating phase composite subjected to a static three-point bending load were investigated in the present study using 2D microstructure-embedded numerical simulation. In particular, the underlying mechanisms of crack initiation and propagation were examined, together with final fracture of the material.

2. Material and methods

2.1. Material and specimen preparation

The SiC_{3D}/Al interpenetrating phase composite used in the present study was fabricated by a liquid metal infiltration technique. Molten Al alloy was infiltrated into a porous SiC ceramic sponge under vacuum conditions to create an interpenetrating network of metal and ceramic. Fig. 1 is an SEM backscattered-image micrograph of the SiC_{3D}/Al composite, in which the dark material is the SiC ceramic (80% by volume), and the lighter grey material is metallic Al (20%).

The three-point bending test specimen (Fig. 2) was an unnotched 50 mm × 2 mm × 6 mm prism. The test was observed by an in situ (SEM). The specimen surfaces were finished to a very high polish in several stages, beginning with coarse 180 grit emery paper, then with successively finer 400, 600, 800, 1200 and 1500 grits, and finally with diamond paste on nylon cloth.

2.2. Testing procedures

An in-situ JEOL JSM-5800 SEM was used to observe crack growth during the test. The loading stage of the SEM allowed the electron beam to navigate and scan the path of the crack as it propagated inside the specimen.

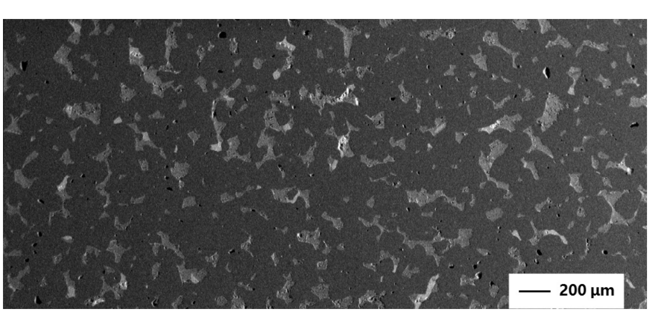

Fig. 1. Micrograph of SiC_{3D}/Al interpenetrating phase composite.

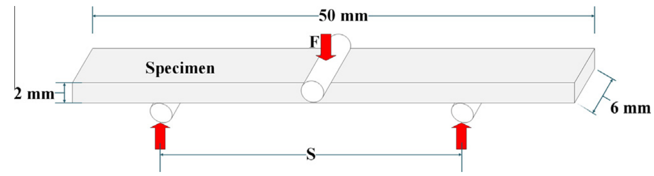

Fig. 2. Schematic of three-point bending test.

The specimen was arranged in a three-point bending configuration for the test (Fig. 2) supported on two steel rollers 30 mm apart (S = 30). A load F was applied via a third roller on the mid-point of the specimen. To simulate quasi-static conditions, the displacement rate was fixed at 0.1 mm/min. The test was performed at room temperature inside the vacuum chamber of the SEM.

3. Finite element numerical simulations

To understand and explain the underlying failure mechanisms and test results, FE numerical simulations using ANSYS LS-DYNA software were performed to predict the nature of the crack growth inside the microstructure.

3.1. Material models and loading condition

In this paper, a rectangular two-dimensional FE model of the test specimen measuring 50 mm × 2 mm was divide into two regions. The vicinity of the crack was modeled into an embedded 4 mm × 2 mm micromodel (Fig. 3(a)), which was used to track the process of crack propagation. While the area far away from the crack was treated with the homogenization method. The micromodel was linked to the macromodel by employing the *CONTACT_TIED_NODES_TO_SURFACE in LS-DYNA, as shown in Fig. 3(b). The width of the specimen (i.e., normal to the plane of the 2-D model) was 6 mm; since the specimen thickness (i.e., in the plane of the 2-D model) was 2 mm, it was assumed that the specimen was constrained in the direction normal to the plane of the model. On this assumption, plane strain elements were chosen for the FE mesh of both the macro- and micromodel; the total number of elements was 101,000.

A displacement rate of 0.1 mm/min was adopted to be consistent with the experimental procedure. For a comparison, the loading curves of testing and numerical simulation are plotted in Fig. 4.

3.2. Parameters in material models

Considering the high content of SiC ceramic (80%, mentioned in Section 2.1) and the small elastic deformation far away from the crack, a linear elastic model was proposed for the macromodel; for the SiC ceramic and metallic Al content of the micromodel, linear elastic model and elastic–plastic material model with kinematic hardening were selected accordingly.

The most common method used to model the elastic behavior of composites is the rule of mixture (ROM) models [18], which involve the Voigt average and the Reuss average. The Voigt average assumes that in a polycrystalline body all grains are subjected to the same uniform strain; for the Reuss average, it is assumed that the stress of each grain is equal to the average stress applied to the material. Using elastic modulus as an example, the equivalent modulus of SiC_{3D}/Al composite can be derived according to Eqs. (1) and (2).

$$E_{\mathrm{Voigt}} = E_{\mathrm{SiC}}\psi_{\mathrm{SiC}} + E_{\mathrm{Al}}\psi_{\mathrm{Al}} \tag{1}$$

$$E_{\mathrm{Reuss}} = 1/(\psi_{\mathrm{SiC}}/E_{\mathrm{SiC}} + \psi_{\mathrm{Al}}/E_{\mathrm{Al}}) \tag{2}$$

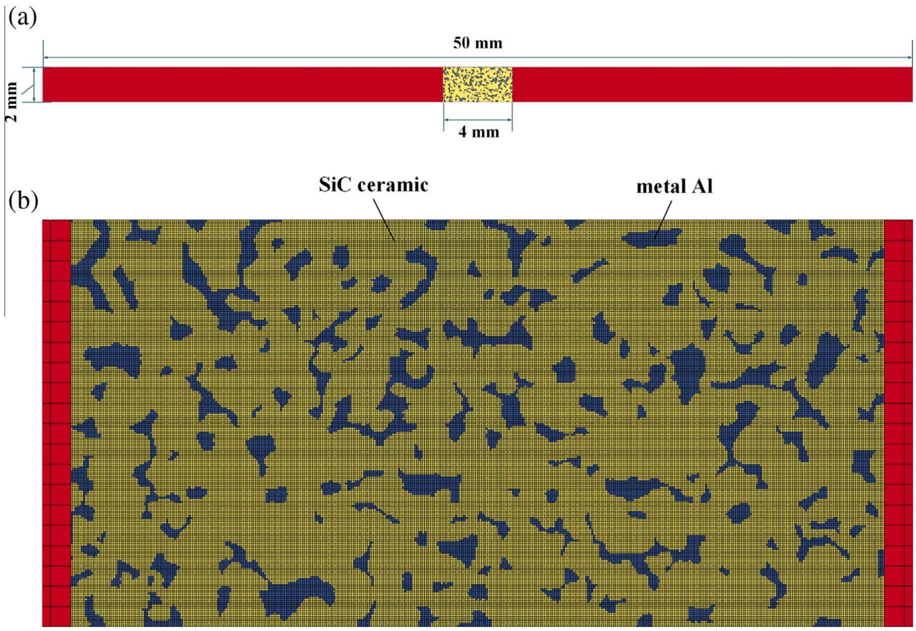

Fig. 3. Finite element model for SiC_{3D}/Al composite: (a) whole model; (b) micromodel.

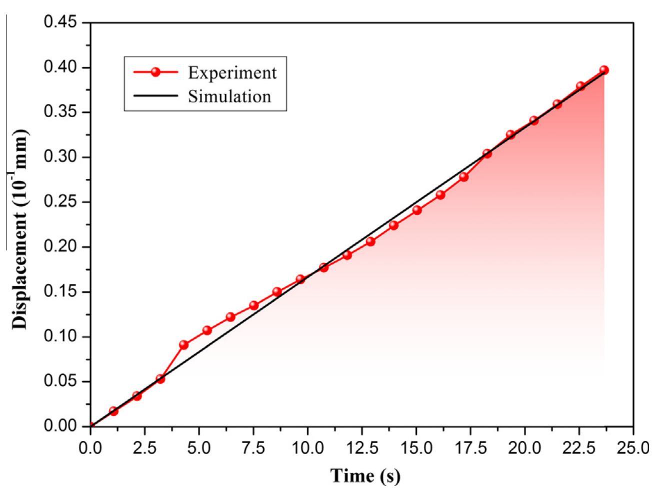

Fig. 4. Comparison of loading curves between testing and numerical simulation.

Table 1
Parameters for linear elastic models.

Material	Density, ρ (g/cm^3)	Elastic modulus, E (GPa)	Poisson's ratio, ν	Failure stress, σ_{max} (MPa)
Macro model	3.05	257	0.3	–
SiC	3.216	450	0.142	450

Table 2
Parameters for elastic–plastic material model.

Material	Density, ρ (g/cm^3)	Elastic modulus, E (GPa)	Poisson's ratio, ν	Yield strength, σ_s (MPa)	Tangent modulus, E_{tan} (MPa)	Failure strain, ε_{max}
Al	2.7	70	0.33	50	250	1

where E and ψ are respectively the modulus and volume fraction of SiC ceramic and metallic Al.

Further study by Hill shows that the Voigt and Reuss models can be used as the upper and lower limits for the average elastic constants, respectively, and the mean of those limits yields values close to measured moduli [19]. Therefore, the average of the upper and lower limits can serve as a suitable estimate for the effective parameters such as the elastic modulus, as well as Poisson's ratio of the macromodel [20]. In addition, the *MAT_ADD_EROSION routine in LS-DYNA was employed to define the failure criteria of the materials. The properties of the three materials are listed in Tables 1 and 2, in which σ_{max}, ε_{max} are respectively the maximum principal stress and maximum principal strain at failure.

4. Results and discussion

4.1. Test and simulation results

In the experimental test, no crack generation was observed initially. With increasing load, the crack propagated rapidly and frac-

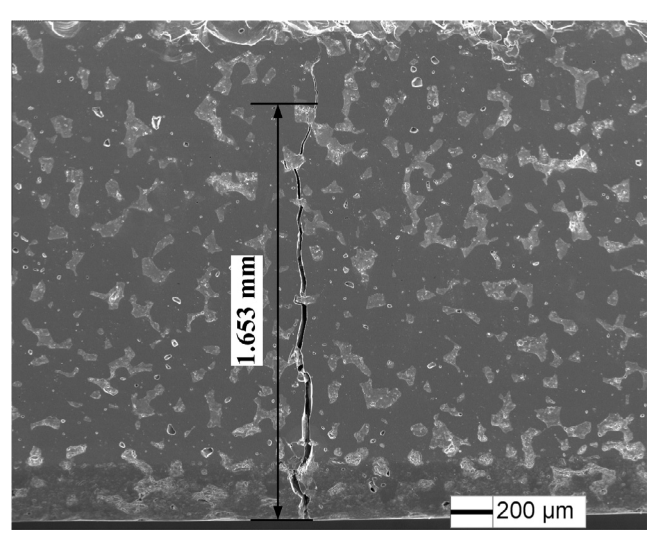

Fig. 5. Micrograph showing primary crack in SiC_{3D}/Al composite.

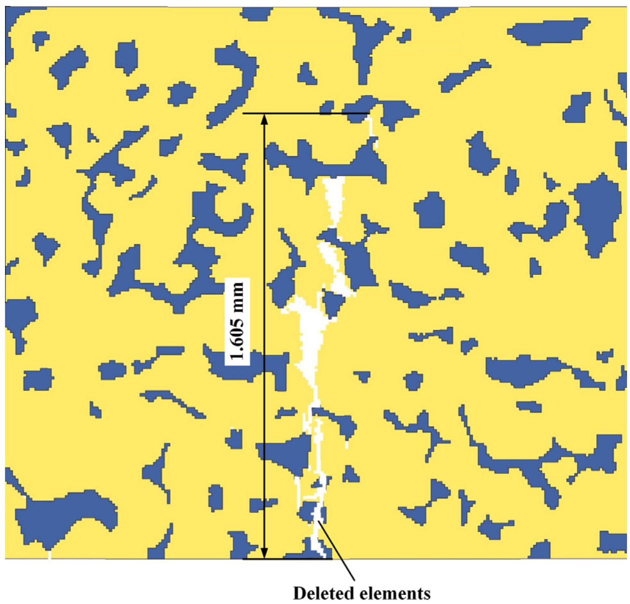

Fig. 6. Simulated crack growth path in SiC_{3D}/Al composite.

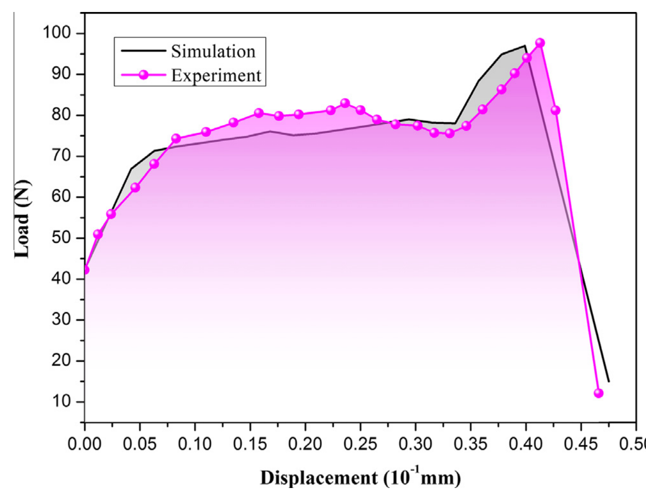

Fig. 7. Comparison of load–displacement curves between testing and numerical simulation.

tured instantaneously at $F = 80$ N, accompanied by a 1.653 mm macrocrack crossing the entire specimen (Fig. 5). As a result, recording the processes of crack initiation and propagation was problematic. From the standpoint of fracture characteristics it was concluded that the fracture of the SiC_{3D}/Al composite material was typical of brittle failure.

However, numerical simulation allowed the whole fracture process to be tracked, from crack initiation and propagation to eventual failure of the composite material. As illustrated in Fig. 6, the deleted elements in the FE model help to visualize the crack growth path which measures about 1.605 mm. The simulation value approaches the experimental result very well.

Both the experimental and simulation results indicated that crack propagation occurred predominantly in the SiC phase, which is consistent with the general understanding that crack propagation occurs in the brittle ceramic phase. The experimental test and the simulation were consistent at the macroscopic scale, with both methods indicating that the primary crack was roughly parallel to the loading direction.

In order to further investigate the validity of the simulation, a quantitative comparison of the load–displacement curves between computation and experiment is also necessary [21]. As shown in Fig. 7, there is a good agreement between the predicted and experimental curves.

4.2. Failure mechanism analysis

Assuming from the above results the validity of the two-dimensional microstructure-embedded numerical simulation, further discussion will now focus on the underlying mechanism of crack initiation, crack propagation and failure of SiC_{3D}/Al composite

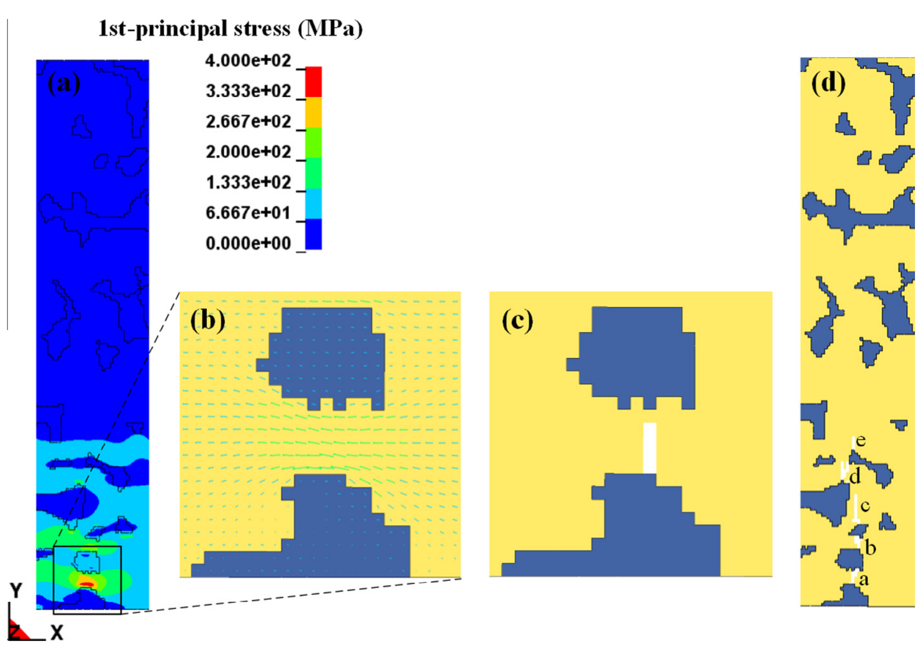

Fig. 8. Simulated crack propagation in SiC_{3D}/Al composite: (a) stress contours of the SiC_{3D}/Al composite at $t = 16.17$ s; (b) stress vectors from inset in Fig. 6(a); (c) crack initiation in SiC phase; (d) further propagation of microcracks.

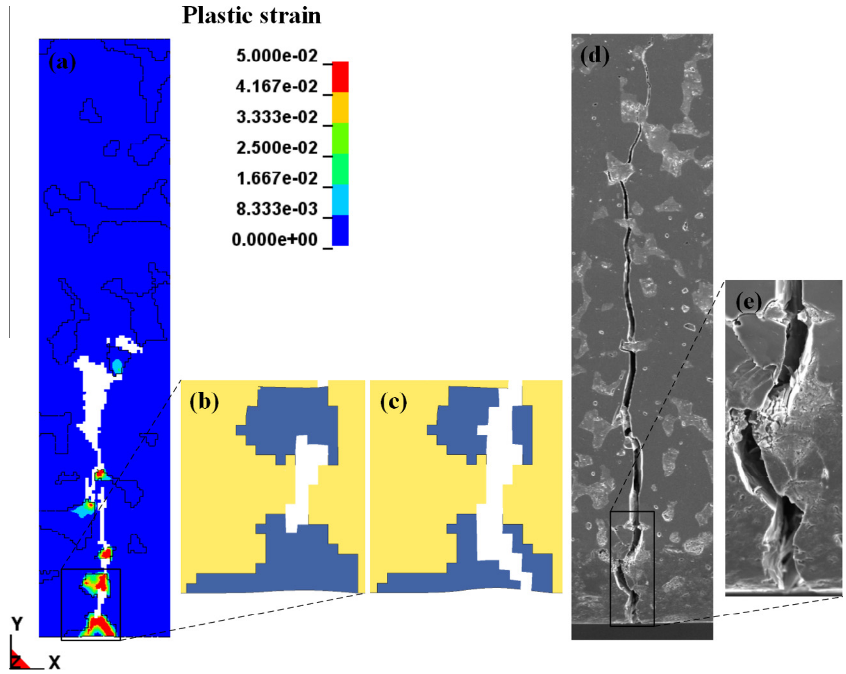

Fig. 9. Crack propagation in SiC_{3D}/Al composite: (a) calculated strain contours of SiC_{3D}/Al composite from simulation at $t = 22.30$ s; (b) simulated failure of Al phase; (c) simulated cracking behavior at bottom of specimen; (d) micrograph showing crack growth path during the test; (e) micrograph showing tearing behavior of the Al phase.

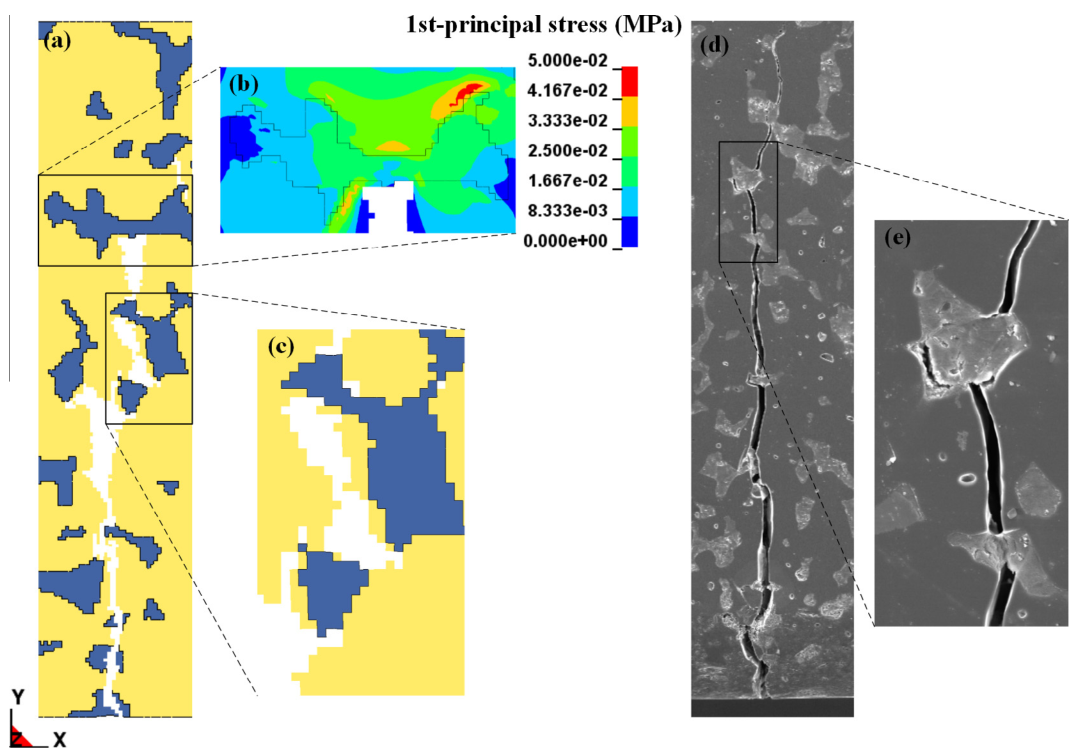

Fig. 10. Crack propagation in SiC_{3D}/Al composite: (a) simulated formation of primary crack; (b) stress contours of the SiC_{3D}/Al composite at $t = 22.9$ s from simulation; (c) simulated examples of cracking behavior along the SiC–Al interface; (d) micrograph showing crack growth path during test; (e) micrograph showing crack bridging over the Al phase.

material subjected to a bending load. This information could not be determined by direct in-situ SEM observation alone.

Fig. 8(a) shows that at time $t = 16.17$ s from initial application of the load, a stress concentration initially occurred in the SiC ceramic phase near the bottom of the specimen where the maximum tensile stress reached 400 MPa. As the applied load continued to increase, the maximum tensile stress eventually exceeded the tensile strength of the SiC, initiating cracking. The stress vectors in Fig. 8(b) (inset in Fig. 6(a)) show the presence of tensile stress in the x-direction. As a result, microcracking was not initiated at

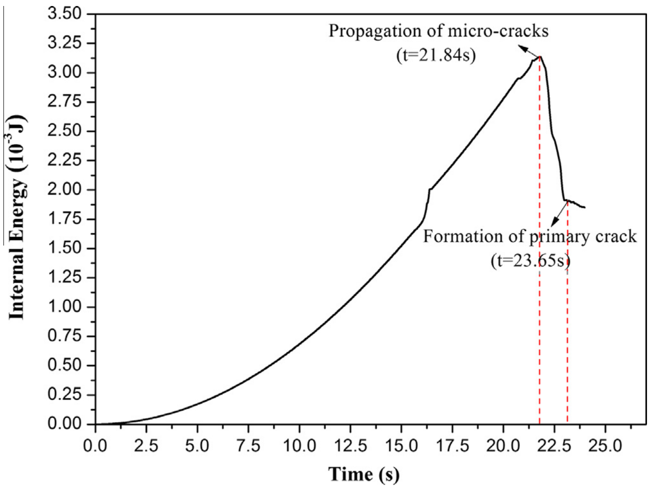

Fig. 11. Internal energy–time curve for SiC_{3D}/Al composite during three-point bending test.

the bottom of the specimen, but rather within the SiC close to a SiC–Al interface. It then propagated vertically, that is, normal to the horizontal tensile stress (Fig. 8(c)); Fig. 8(d) shows that further propagation occurred as loading increased. At t = 21.76 s, the number of microcracks increased to five (a, b, c, d, e in Fig. 8(d)), all within the SiC phase.

Fig. 9(a) shows the strain contours at t = 22.30 s. It was observed that the Al phase at the bottom of the specimen experienced severe tearing plastic deformation, which caused the Al phase to fail (Fig. 9(b)). The penetrative crack at the bottom of the specimen, shown in Fig. 9(c), occurred at t = 23.40 s. Fig. 9(d) and (e) are micrographs of the crack growth path during the test. They confirm the tearing of the Al phase at the bottom of the specimen, as well as the accuracy of the numerical simulation results.

Subsequently, the generated microcracks propagated and amalgamated at t = 23.65 s to form a primary crack, as shown in Fig. 10(a). The primary crack then propagated rapidly until the specimen ruptured. It was noted that the crack was finally terminated at a SiC–Al interface due to the greater plasticity of the Al phase that enabled it to deform at that point without cracking.

Fig. 10(b) (inset in Fig. 10(a)) shows the stress contours of the SiC_{3D}/Al composite at t = 22.9 s, where it is seen that a new stress concentration developed within the SiC above the Al phase, such that the primary crack bridged over the Al phase, then continued to propagate within the SiC ceramic material.

The internal energy–time curve of the SiC_{3D}/Al composite derived from the model simulation (Fig. 11) implies that, as the applied load increased, the accumulated strain energy in the composite gradually elevated the total internal energy to a peak at t = 21.84 s, then, with further microcrack propagation and formation of the primary crack, the internal energy of SiC_{3D}/Al was rapidly released and, at t = 23.65 s, dropped to 60% of the peak. Thus, according to the simulation results, at the end stage of the primary crack, cracking no longer occurred within the Al. The simulation results also indicated some cracking behavior along the SiC–Al interface due to the relatively weaker local strength, as shown in Fig. 10(c). Fig. 10(d) and (e) are micrographs of the crack growth path in SiC_{3D}/Al composite after the experimental test. It is clearly seen that, before the primary crack was arrested, it propagated along the SiC–Al interface for some distance before bridging over the Al phase, in close agreement with the numerical simulation.

5. Conclusions

The fracture characteristics and failure behavior of SiC_{3D}/Al interpenetrating phase composite subjected to a static three-point bending load were monitored by an in-situ SEM at the microstructural level. A microstructure-embedded finite element model was also used to simulate and predict the behavior of the material under the same circumstances. The numerical simulation results were consistent with the observed experimental results.

It was found that microcracking was not initiated at the bottom of the specimen, but rather within the SiC close to a SiC–Al interface due to an initial stress concentration at that location. As loading increased, the number of microcracks increased within the SiC phase until the Al phase at the bottom of the specimen experienced severe tearing plastic deformation and failed. Subsequently, the generated microcracks propagated and amalgamated to form a primary crack. Noticeably, before the primary crack finally terminated at a SiC–Al interface, it was found to bridge over the Al phase and continue to propagate within the SiC ceramic material. According to the simulation results, at the end stage of the primary crack, cracking no longer occurred within the Al due to the rapid release of the internal energy and the greater plasticity of the Al phase.

Acknowledgement

We gratefully acknowledge the financial support of the program for New Century Excellent Talents in University (NCET-12-0051).

References

[1] D.R. Clarke, J. Am. Ceram. Soc. 75 (1992) 739–759.
[2] P. Agrawal, C.T. Sun, Compos. Sci. Technol. 64 (2004) 1167–1178.
[3] C. Periasamy, R. Jhaver, Mater. Sci. Eng. A 527 (2010) 2845–2856.
[4] G. Pezzotti, O. Sbaizero, Mater. Sci. Eng. A 303 (2001) 267–272.
[5] M. Hoffman, S. Skirl, Acta Mater. 47 (1999) 565–577.
[6] J. Rahul, T. Hareesh, Mater. Sci. Eng. A 499 (2009) 507–517.
[7] C. San Marchi, M. Kouzeli, Scr. Mater. 49 (2003) 861–866.
[8] M.C. Breslin, J. Ringnalda, Mater. Sci. Eng. A 195 (1995) 113–119.
[9] S. Vaucher, J. Kuebler, O. Beffort, Compos. Sci. Technol. 68 (2008) 3202–3207.
[10] L.D. Wegner, L.J. Gibson, Int. J. Mech. Sci. 42 (2000) 943–964.
[11] M.J. Hadianfard, Y.W. Mai, J. Mater. Sci. 30 (1995) 5335–5346.
[12] M.X. Gao, Mater. Lett. 58 (2004) 1761–1765.
[13] H. Prielipp, M. Knechtel, N. Claussen, Mater. Sci. Eng. A 197 (1995) 19–30.
[14] W. Zhou, Mater. Lett. 40 (1999) 156–160.
[15] Q.L. Dai, Z.P. You, J. Eng. Mech. 133 (2007) 163–173.
[16] W. Shen, Surf. Coat. Technol. 205 (2011) 2964–2969.
[17] A.Y. Yin, X.H. Yang, Eng. Fract. Mech. 78 (2011) 2414–2428.
[18] K.K. Chawla, Composite Materials Science and Engineering, second ed., Springer, New York, 1998.
[19] R. Hill, Proc. Phys. Soc., Sect. A 65 (1952) 349–354.
[20] T.E. Wilkes, B.J. Harder, Acta Mater. 57 (2009) 6234–6242.
[21] G.W. Zeng, X.H. Yang, Constr. Build. Mater. 55 (2014) 323–332.